

On Geometric Understanding and Learned Data Priors in VGGT

Jelena Bratulić^{1*}, Sudhanshu Mittal¹, Thomas Brox¹, Christian Rupprecht²

¹ University of Freiburg, ² University of Oxford

bratulic@cs.uni-freiburg.de

Abstract

The Visual Geometry Grounded Transformer (VGGT) is a 3D foundation model that infers camera geometry and scene structure in a single feed-forward pass. Trained in a supervised, single-step fashion on large datasets, VGGT raises a key question: does it build upon geometric concepts like traditional multi-view methods, or does it rely primarily on learned appearance-based data-driven priors? In this work, we conduct a systematic analysis of VGGT’s internal mechanisms to uncover whether geometric understanding emerges within its representations. By probing intermediate features, analyzing attention patterns, and performing interventions, we examine how the model implements its functionality. Our findings reveal that VGGT implicitly performs correspondence matching within its global attention layers and encodes epipolar geometry, despite being trained without explicit geometric constraints. We further investigate VGGT’s dependence on its learned data priors. Using spatial input masking and perturbation experiments, we assess its robustness to occlusions, appearance variations, and camera configurations, comparing it with classical multi-stage pipelines. Together, these insights highlight how VGGT internalizes geometric structure while using learned data-driven priors.

1. Introduction

Estimating 3D geometry from a set of 2D images has long been a fundamental challenge in computer vision. The traditional way relies on rigorous, geometry-constrained pipelines that require a multi-step, sequential process from extracting, matching, and refining local features to estimating camera parameters and reconstructing 3D point clouds. This approach, although mathematically precise, struggles with ambiguities and lacks robustness to scene dynamics during feature matching and error accumulation due to partial visibility. This is because it is hard for the approach to include priors about the scene apart from camera geometry.

*The work was done during a PhD visit to the University of Oxford within the ELLIS PhD program.

Moreover, pipelines are typically slow because they rely on runtime optimization.

Recent successes in deep learning, such as DUS3R [29], MAS3R [15], and VGGT [28], have shown that 3D reconstruction can be achieved in a single unified feed-forward step, effectively replacing the traditional multi-stage pipeline. These methods predict camera poses and dense 3D point maps from image sequences using a functional mapping learned from large datasets. As all optimization is shifted to training, they run much faster than classical frameworks, and the priors learned from the data make them significantly more robust to ambiguities and input variations. However, learned functional mappings are prone to fail in out-of-distribution cases. As the above models are trained on millions of samples, it is hard to track when a model acts out-of-distribution and how badly it fails in such cases. It is worth noting that the laws of 3D geometry are universal and should not depend on the distribution of the training data. Therefore, the question arises, if these networks, while learning from data, pick up the underlying generic geometric processes and use them in some form in their functional mapping. This would guarantee a similar robustness to out-of-distribution cases as with traditional pipelines, while profiting from the complex data priors when run in-distribution.

In this work, we examine the underlying mechanisms of one of these feed-forward 3D reconstruction models: VGGT. We aim to shed some light on the mechanistic way of how this model computes its outputs. In particular, we are interested in whether the network uses some of the universal principles of 3D geometry, such as correspondences and epipolar geometry. To this end, we design a controlled study using different versions of a synthetic dataset built from ShapeNet [6] objects under various conditions, with complete scene information and all 3D attributes being available. Our systematic analysis adopts two perspectives: (1) a **geometrical** perspective, where we probe the internal representations and perform interventions to assess the causal effect of these representations on the fidelity of the network’s representation in terms of epipolar geometry, (2) a **data** perspective, where we test the model’s robustness

to interventions on the input image to study the (typically positive) influence of learned data-driven priors.

VGGT directly predicts camera parameters, point maps, depth maps, and 3D point trajectories, and is jointly optimized across all these tasks via task-specific heads. To study the model’s use of geometric principles, we focus on a fundamental property of 3D geometry – epipolar geometry. The fundamental matrix $\mathbf{F} \in \mathbb{R}^{3 \times 3}$ provides a natural lens for this investigation, as it formalizes the epipolar geometry between different camera views and corresponding points observed in them. Since VGGT is not explicitly optimized for fundamental matrix estimation, we can use it as a proxy for understanding how much the model has learned to use geometric constraints by probing its internal representations for information that yields the fundamental matrix.

Contributions. Our analysis reveals several key insights. (1) The fundamental matrix can be recovered from the model’s intermediate representation. (2) We can also localize in which layers of the network the information about the epipolar geometry becomes available. The ability to estimate the fundamental matrix from the layer’s representations coincides with the availability of point correspondences in the attention space. (3) Through targeted attention-knockout interventions, we establish a causal link between middle layers, with strong correspondence matching capability, and the representation of epipolar geometry. (4) From a data perspective, we demonstrate that VGGT handles challenging scenarios with scene ambiguity with greater robustness compared to classical methods.

2. Related work

Classical 3D reconstruction and epipolar geometry. Classical structure-from-motion (SfM) pipelines [1, 12, 23, 24] include different stages: feature detection, matching, camera pose estimation, and bundle adjustment, in which they rely on hand-crafted features from algorithms such as SIFT [17]. The fundamental matrix \mathbf{F} forms the mathematical foundation of epipolar geometry [12], where it can be estimated through classical algorithms such as the five-point [19] or the eight-point [11] algorithms, enabling estimation from minimal available correspondences. These estimation algorithms are usually accompanied with geometric algorithms like RANSAC [9] for handling noisy correspondences and outliers. Recently, learned matching methods such as SuperGlue [22], LightGlue [16], and LoFTR [26] have improved correspondence matching while the estimation of the Fundamental matrix still relies on classical algorithms. Epipolar geometry is an ideal probe for studying model’s geometric understanding as it is mathematically precise and algorithmically well-defined.

Learned 3D reconstruction models. Recent deep learning approaches challenge the traditional multi-stage paradigm for 3D reconstruction. DUS3R [29] proposed

a novel transformer-based approach for dense and unconstrained stereo 3D reconstruction without known camera poses by directly predicting aligned point clouds from image pairs, but it requires costly test-time alignment. MAST3R [15] further improves the matching capabilities in case of large viewpoint difference and preserves the robustness of DUS3R by adding a dense local features head. VGGSfM [27] demonstrated that fully differentiable end-to-end model outperforms classical methods. VGGT [28] represents the current state-of-the-art directly predicting camera poses, depths, point clouds and 3D point tracks in a single feed-forward pass while also reporting significantly faster inference. Follow-up work further accelerates inference time [30] or extends the architectures to other downstream tasks [18, 33]. Despite these advances, the understanding of the internal working mechanisms remain unexplored – a gap our work addresses.

Interpretability and causal analysis. Understanding neural network mechanisms has become increasingly important with much work centered around LLMs [8, 20]. One common approach to getting a better understanding of a model is to leverage probing classifiers [2, 5, 14] to assess whether the information is linearly decodable from representations. For computer vision tasks, Network Dissection and related work [3, 4, 32] quantify the CNNs’ uncertainty at individual units, whereas Chefer et al. [7] showed that naive attention visualization can be misleading for transformers. Different interventions, such as activation patching or causal mediation analysis [13, 31], provide more substantial evidence by measuring the effects of modified activations within a model. However, limited work has been done in interpretability research on geometric understanding in 3D vision models, as most interpretability work focuses primarily on discriminative tasks or generative modeling. Our work uses interventions via attention knockouts to uncover the relation between correlated observations in VGGT and to establish which components causally drive the geometric understanding and the model’s predictions. Concurrently with our work, Stary et al. [25] analyze a variant of the DUS3R model and provide insights its internal state, as well as the role of individual layers and correspondences.

3. Background

3.1. Epipolar Geometry

Here we provide a brief overview on the epipolar geometry, but an extensive analysis can be found in [12]. Epipolar geometry describes the projective relationship between two cameras viewing the same 3D point. If a 3D point $\mathbf{X} \in \mathbb{R}^3$ is observed by two pinhole cameras, its image projections are

$$\mathbf{x}_1 = \mathbf{K}_1[\mathbf{I} \mid \mathbf{0}]\mathbf{X}, \quad \mathbf{x}_2 = \mathbf{K}_2[\mathbf{R} \mid \mathbf{t}]\mathbf{X}, \quad (1)$$



Figure 1. Few samples from our synthetic controlled dataset build from ShapeNet [6] objects.

where \mathbf{K}_i are the camera intrinsics and (\mathbf{R}, \mathbf{t}) is the relative pose. A ray from the first camera center through \mathbf{x}_1 defines an *epipolar plane* with the two camera centers. Its intersection with the second image plane gives the *epipolar line* ℓ_2 , on which the corresponding point \mathbf{x}_2 must lie. All epipolar lines intersect at the epipole. This geometric relationship is expressed by the *epipolar constraint*:

$$\mathbf{x}_2^\top \mathbf{E} \mathbf{x}_1 = 0, \quad \mathbf{E} = [\mathbf{t}]_\times \mathbf{R}, \quad (2)$$

where \mathbf{E} is the *essential matrix* and $[\mathbf{t}]_\times$ is the skew-symmetric matrix representing the cross product with \mathbf{t} . For uncalibrated cameras, the relation becomes

$$\mathbf{x}_2^\top \mathbf{F} \mathbf{x}_1 = 0, \quad \mathbf{F} = \mathbf{K}_2^{-\top} \mathbf{E} \mathbf{K}_1^{-1}, \quad (3)$$

where \mathbf{F} is the *fundamental matrix*.

Both the essential matrix \mathbf{E} and fundamental matrix \mathbf{F} have rank 2, as $\mathbf{E} = [\mathbf{t}]_\times \mathbf{R}$ inherits the rank deficiency from the skew-symmetric matrix $[\mathbf{t}]_\times$. This constraint reflects the fact that all epipolar lines intersect at the epipole. When estimating \mathbf{F} from point correspondences, the rank-2 constraint is typically enforced by projecting the unconstrained solution onto the manifold of rank-2 matrices. Given an initial estimate $\hat{\mathbf{F}}$, we compute its singular value decomposition $\hat{\mathbf{F}} = \mathbf{U} \text{diag}(\sigma_1, \sigma_2, \sigma_3) \mathbf{V}^\top$ where $\sigma_1 \geq \sigma_2 \geq \sigma_3$, and set the smallest singular value to zero:

$$\mathbf{F} = \mathbf{U} \text{diag}(\sigma_1, \sigma_2, 0) \mathbf{V}^\top. \quad (4)$$

This produces the closest rank-2 approximation in the Frobenius norm.

Evaluating Epipolar Geometry. We can assess the quality of an estimated fundamental matrix using two metrics that quantify deviations from epipolar consistency.

The algebraic error

$$e_{\text{alg}} = \mathbf{x}_2^\top \mathbf{F} \mathbf{x}_1 \quad (5)$$

measures the constraint satisfaction (which should be 0), but has no geometric meaning directly and is scale dependent. More geometrically meaningful measures are the Sampson error and the smallest singular value of \mathbf{F} . The *Sampson error* [21] represents a first-order geometric approximation of true geometric error:

$$d_{\text{Sampson}} = \frac{(\mathbf{x}_2^\top \mathbf{F} \mathbf{x}_1)^2}{\|(\mathbf{F} \mathbf{x}_1)_{1:2}\|^2 + \|(\mathbf{F}^\top \mathbf{x}_2)_{1:2}\|^2} \quad (6)$$

Sampson error approximates the reprojection error, avoiding iterative optimization. In practice, good geometric consistency for well-calibrated systems should have Sampson error below 1–2 pixels, though acceptable values depend on image resolution, focal length and the purpose of application and precision. The *smallest singular value* of \mathbf{F} must be zero to satisfy the rank-2 constraint of the fundamental matrix. In practice, the smallest singular value that is less than 10^{-3} of the largest singular value is generally considered acceptable. These metrics serve as key indicators of the epipolar geometric understanding of models such as VGGT.

3.2. Visual Geometry Grounded Transformer (VGGT)

Visual Geometry Grounded Transformer (VGGT) [28] is a feed-forward neural network following the transformer architecture. It jointly predicts all 3D attributes of a scene from one, a few, or hundreds of views provided in a sequence in a matter of seconds. Given patch-tokenized images aligned with the DINOv2 model, VGGT yields camera extrinsics and intrinsics, point maps, depth maps, and 3D point trajectories across views. The model leverages the DINOv2 backbone with additional frame-wise and global self-attention layers to combine both local and global cross-view features and task-specific heads. VGGT was trained on a large mixture of publicly available 3D datasets using direct supervision for camera pose estimation, depth prediction, 3D point cloud reconstruction, and 3D point tracking on sequences of 2–10 images. The reconstruction is aligned to the coordinate system of the first camera.

We utilize the original model, which is based on a publicly available checkpoint consisting of 24 alternating frame-wise and global self-attention blocks, and employs DINOv2 Large with a patch size of 14. All the images are of size 518x518, so each image is tokenized into 37x37 or 1369 tokens. Each view also has one camera token and four register tokens. We use the model only in inference mode.

3.3. Dataset Design

To probe VGGT’s geometric understanding and model different scenarios, we generated a controlled synthetic dataset from ShapeNet [6] assets rendered in Blender, as it enables precise control over scene properties and eliminates complex scene ambiguities that could bias our analysis of the

model’s internal workings. This setup provides flexibility to systematically modify input conditions such as occlusions, lightning, and viewpoint differences in the scene. We selected two types of objects: 10 different categories of *unique* assets with distinctive features and 5 different categories of *symmetric* assets (e.g., bottles, vases) that introduce correspondence ambiguity. We show 3 pairs of assets in Fig. 1 Each scene was rendered with three-point lighting under various camera configurations regarding focal length, angular distance between the cameras, and scene composition. We used focal lengths ranging from 24 mm to 100 mm with a standard 36 mm camera sensor. We distinguish between 4 camera configurations: a stereo setup with parallel image planes and a horizontal baseline, and three different non-parallel image planes with different angular baselines, categorized as small (10 - 25 degrees), medium (45 - 75), and large (90 - 120). For robustness experiments, we created ambiguous scenes with repetitive objects. This setup provides complete geometric ground truth (camera parameters, depth, correspondences, fundamental and essential matrices) for precise analysis. We provide more details about the dataset and the scenes in the supplementary.

4. Geometrical interpretability in VGGT

VGGT is trained on multiple objectives, including camera pose estimation, depth prediction, and 3D tracking. To investigate whether the model develops geometric reasoning beyond these supervised tasks, we examine its ability to represent the fundamental matrix—a core geometric structure relating corresponding points across views that was never explicitly supervised during training. Further, we analyze how point correspondences across views are captured within the model’s internal representations and how they contribute to this geometric structure.

4.1. Does VGGT encode geometry? If so, where?

We probe VGGT’s intermediate layers to determine where, and to what extent, the fundamental matrix can be recovered from these representations.

Experiment setup. We train simple two-layer MLP probes on VGGT’s camera tokens at each layer to predict the fundamental matrix. Each probe utilizes a hidden dimension of 512 and is optimized for 50 epochs using the squared Sampson distance as the training loss on ground-truth correspondences, without directly enforcing the rank-2 constraint. We train probes on different camera sampling modes and focal lengths. We report the root Sampson error in pixel space across 4 unseen data splits: val and test splits containing training categories in novel scenes; novel objects and symmetric objects containing unseen categories with differences in object symmetry. Additional details and results are provided in the supplementary.

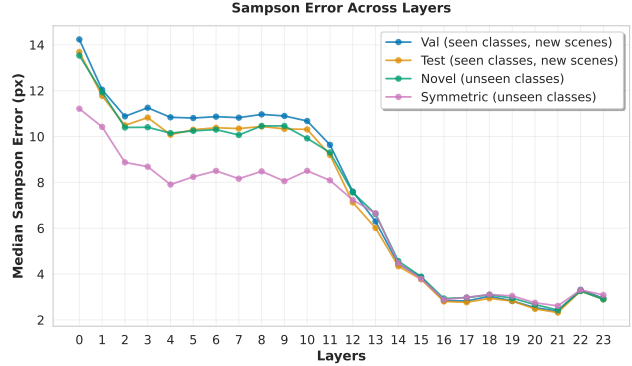


Figure 2. **Probing VGGT’s internal representations for fundamental matrix approximation.** We observe a clear transition beginning in the middle layers and strong recovery performance in the final layers across different data splits.

Results. Figure 2 shows that starting in the middle layers (around layer 12), VGGT comprises a representation that allows fundamental matrix recovery. Performance continues to be refined through the final layers. The sudden drop in error within a few layers suggests that an important requirement for establishing this information develops just within these layers. As a second criterion, we also check the smallest singular value of the predicted F . We observe that it reaches the minimum in the same set of layers and is approximately $2.5e-4$ smaller than the largest value, further supporting the emergence of epipolar geometry within these layers (see supplementary). An obvious candidate for this requirement is that the network’s attention maps are internally capturing a correspondence structure across views. How interpretable these structures are in the representation space is not yet clear under this probing scheme.

Epipolar geometry becomes represented from the middle layers onward and is refined toward the final layers.

4.2. How do attention maps encode correspondences?

Probing reveals the emergence of learned epipolar geometry in the intermediate layers. Yet, so far, we do not know how the model recovers this information. To this end, we aim to discover the underlying correspondence-matching patterns in the attention maps of those layers across two views. We hypothesize that these correspondences are computed within VGGT’s global attention layers.

Experiment setup. We analyze the query-key (QK) attention space to identify correspondence matching. For each patch token in the source image, we locate the patch in the target image that receives the highest attention and

calculate accuracy based on whether this target patch corresponds to the true matching patch. When a source patch maps to multiple target patches due to patch discretizations, we count a hit if any of the correct positions receive the maximum attention. We evaluate all unique patch correspondence pairs and report the average correspondence accuracy over a test set of 5 scenes from different object categories, taken at a 50 mm focal length, averaged across sampling modes that cover different camera-pair configurations. Additional details are in the supplementary.

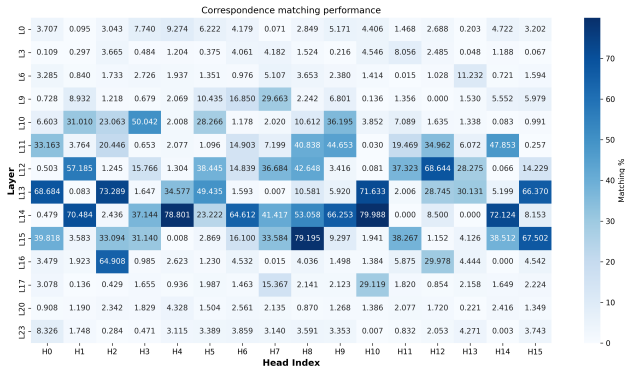


Figure 3. **Correspondence matching per attention head.** Strong matching performance establishes in the middle layers starting at layer 10, immediately preceding the transition observed in Fig. 2.

Results. Figure 3 shows that the middle layers from 10 to 16, provide strong correspondence matching across multiple attention heads. This capability starts to establish at layer 10, a few layers before the sharp improvement in fundamental matrix recovery at layers 13 and 14. This suggests a connection between correspondence estimation and the emergence of epipolar geometry within the network.

Point correspondence matching appears in the mid-layer attention heads as a key mechanism, enabling geometric alignment across views.

4.3. Do these attention patterns play a causal role?

The previous observations establish a correlation between the emergence of epipolar geometry via fundamental matrix recovery and the occurrence of correspondence-matching patterns in the same set of intermediate layers. To determine whether the attention patterns are truly a cause for the geometric understanding, we perform targeted interventions on the attention heads that we hypothesize to be a cause for the epipolar representation.

Experiment setup. We intervene on the QK attention space using attention knockout, a method similar to Geva et al. [10], where we zero out weight matrices for specific layer-head combinations of the whole attention map. We

select interventions based on correspondence-matching performance, including two baseline conditions targeting random early and late layers. We report median results across all sampling modes at 50 mm focal length over the test set of 5 scenes. More combinations are in the supplementary.

Results. Figure 4 demonstrates clear causal effects. Disrupting attention in the middle layers degrades Sampson distance error to such a large degree that it can be regarded as a complete failure. Intervening on early or late layers, on the other hand, has no significant impact. Notably, zeroing even a single layer with two heads that show strong correspondence performance causes measurable degradation.

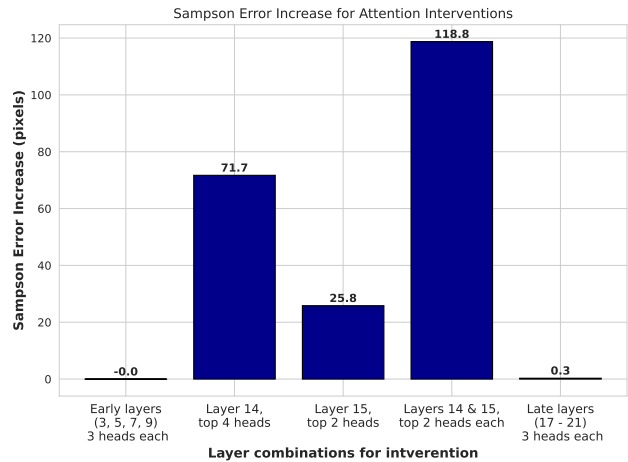


Figure 4. **Performance degradation under attention interventions.** Disrupting early or late layers has minimal impact on performance, whereas middle-layer interventions cause significant degradation. Even two heads in a single layer with strong correspondence matching suffice to impair geometric understanding.

This confirms our hypothesis: directly switching off the attention heads in the middle layers with maximum correspondence performance results in significant degradation in encoded epipolar geometry. Although the dropped attention heads showed strong correspondence matching performance, this observation does not conclusively demonstrate that correspondence matching itself is directly responsible for the emergence of epipolar geometry. These heads may also encode other mechanisms that contribute to the effect.

Intervening on the attention patterns for point correspondences shows a causal relationship between those attention heads and the epipolar geometry representation by the model.

5. The role of learned priors in VGGT

VGGT is a model trained on large, diverse datasets with strong 2D spatial augmentations. This raises an impor-

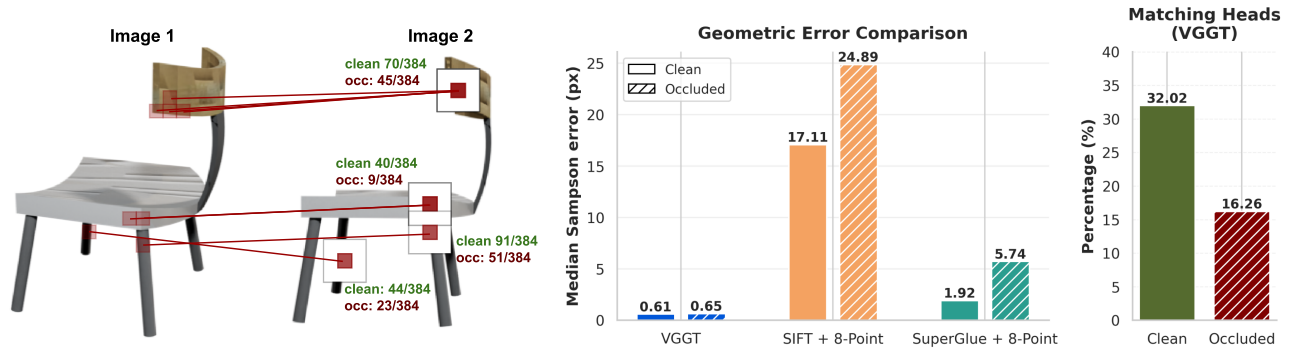


Figure 5. **Occlusion experiment.** (Left) We occlude image two from a pair with white patches and report the correspondence matching ability in all layers only for the masked patches. The occluded model shows lower matching performance yet remains above zero. (Center) We measure the changes in the Sampson error for clean and occluded image pairs where VGGT has a minimal degradation in performance, but others are significantly affected. (Right) We show the average number of heads with correspondence matching on occluded patches for clean and occluded model.

tant question: to what extent does the model’s advantage come from appearance-based priors learned from the training data? And consequently, how much do these capabilities generalize beyond the training distribution? To explore this, we systematically evaluate the robustness of VGGT’s geometric predictions under controlled input perturbations. We consider (i) appearance-based 2D perturbations, such as occlusions, and (ii) rendered 3D perturbations with structural ambiguities, light-source, and camera configuration changes. To assess the model’s robustness, we compare VGGT against classical geometry-based methods and learned correspondence methods.

5.1. How well does VGGT handle occlusions?

To evaluate how well VGGT performs under missing visual information, we examine the impact of occlusions on both correspondence matching and resulting geometric predictions. We simulate occlusions by masking key regions of the image. In principle, the model could address this challenge in multiple ways: by utilizing global geometric reasoning, inferring missing information from learned priors, or simply ignoring the occluded areas.

Experiment setup. We intervene on input images by randomly selecting patches with known correspondences and masking them along with their surrounding regions (3×3 patch neighborhoods); see Fig. 5. We perform inference twice: first on the clean image pair and then on a pair in which one image is partially occluded. We report the change in Sampson distance error (in pixels) and the number of attention heads in which the correspondence is matched, averaged over all intervened correspondences in a scene. Results are averaged over 40 scenes at 50 mm focal length with small viewpoint differences (10-25 degrees). We also compare VGGT’s performance with the 8-point al-

gorithm on all matched correspondences from SIFT [17] and SuperGlue [22].

Results. Figure 5 (left) shows the results of one case where we masked four object patches to be analyzed for occlusion, together with their corresponding ground truth patches. For each occluded patch, we show the number of heads in which the occluded correspondence was matched (green for the clean version and red for the occluded version). Correspondence matching, measured by the number of heads performing the matching (a maximum of 24 layers \times 16 heads = 384 heads), shows that matched heads drops for the corrupted patches but does not collapse entirely.

Figure 5 (right) reports the average number of matching heads before and after occlusion for the occluded patches. While there is a clear drop in matching heads, around 50% heads are still retained, indicating that the model does not ignore the occluded regions but recovers correspondences through some form of inpainting or hallucination.

Additionally, VGGT shows only a slight degradation in the Sampson error, indicating that the epipolar geometry is still restored, whereas the other baselines show clear degradation, shown in Figure 5 (center).

VGGT shows robustness to occlusions, preserving epipolar geometry by partially recovering matching heads for the occluded correspondences.

5.2. How robust is VGGT to scene perturbations?

Traditional multi-view geometry methods rely on locally unique correspondences and therefore degrade in noisy and difficult scenarios. Although VGGT is claimed to be robust to these challenges, this has not been systematically tested. Here, we evaluate VGGT on challenging cases that

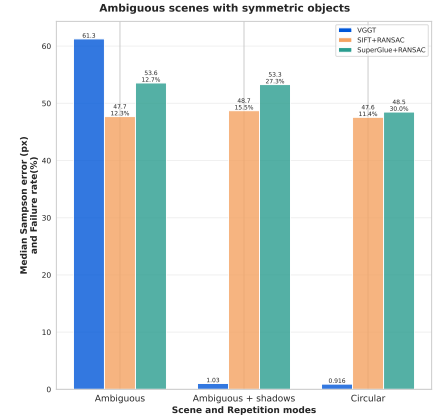
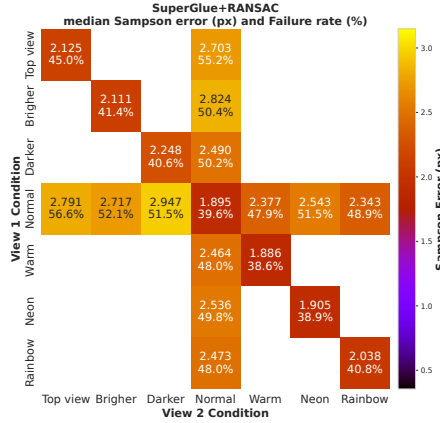
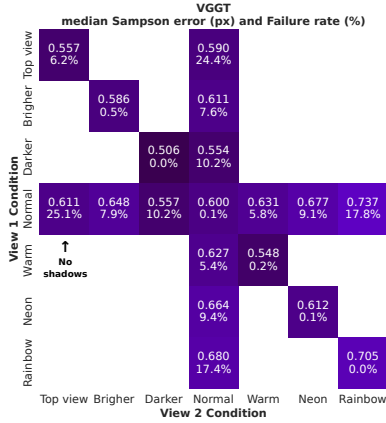


Figure 6. **Light and color robustness.** We compare VGGT against SuperGlue + RANSAC on large viewpoint changes. VGGT shows only slight degradation under the changes, while SuperGlue shows higher sensitivity and a larger failure rate. However, VGGT’s failure rate (Sampson error larger than 10 pixels) increases under extreme lighting changes and shadow variations.

Figure 7. **Ambiguous scenes with repetitions.** VGGT outperforms baselines, even when only shadows disambiguate symmetric objects, but fails on completely ambiguous scenes without shadows.

require reliable local matching and strong global spatial reasoning. We compare it against the classical SIFT + 8-point + RANSAC [17] pipeline as well as a learned matching method SuperGlue [22]. Figure 8 shows some examples of simulated challenging scenarios.

Lighting and color variations. We design controlled experiments to test robustness under diverse lighting conditions by replacing the standard three-point illumination with darker, brighter, and top-lit configurations, as well as colored lighting that alters object appearance. We evaluate both asymmetric (one image modified) and symmetric (both images modified) conditions by comparing median Sampson errors in pixels on success cases and report failure rates for VGGT and the SuperGlue + RANSAC, where failure is an invalid model output or a Sampson error greater than 10 pixels. We show modifications in the supplementary.

Figure 6 shows the performance on medium viewpoint differences for VGGT and SuperGlue. VGGT demonstrates superior robustness compared to classical methods, likely due to the strong color augmentation used in training, with its performance practically unchanged and with a low failure rate. SuperGlue and other baselines have a high failure rate, and their performance is affected by these changes. However, VGGT exhibits a higher failure rate under large lighting and color changes, particularly for top-view lighting, which removes shadows from the scene, and for neon and rainbow lighting, which introduces color inconsistencies. However, when the same interventions are applied to both views, VGGT performs well. It is specifically the case where only one view is intervened, it fails (Sampson error over 10 pixels) more often than for other modifications.

Repetition and symmetry. We generate challenging scenes with multiple instances of the same object arranged in circular pattern. We distinguish between unique (easier) and fully symmetric objects, such as bottles and vases (harder), where geometric ambiguity arises. We present our results for symmetric objects in Fig. 7, where even with asymmetric lighting that creates shadows that break symmetry, classical methods fail to establish reliable correspondences, whereas VGGT effectively leverages these subtle cues. For completely ambiguous scenes with symmetric objects and symmetric lighting, all methods fail as expected, confirming the task is geometrically underconstrained.

Focal length variations. Focal length changes effectively zoom in or out, altering feature scales and correspondence difficulty. We test focal lengths from 24 mm to 100 mm (36 mm sensor) across different viewpoint difference configurations. We compare focal lengths of 35 mm, 50 mm, and 85 mm for the configuration with large viewpoint differences (90 - 120 degrees) on Fig. 9, which shows that VGGT maintains consistent performance across all focal lengths, while classical methods exhibit high failure rates, particularly at extreme focal lengths and significant viewpoint differences. For close stereo pairs, classical methods achieve lower median error when successful, but VGGT demonstrates superior robustness by consistently producing valid predictions. Additional results in supplementary.

VGGT exhibits superior robustness to appearance variations, focal-length changes, and scene ambiguity compared to classical methods, suggesting learned geometric principles generalize well.



Figure 8. **Few simulated examples for robustness analysis.** Neon light changes (left) corresponds to *View 1 normal - View 2 neon* setup from Fig. 6, repetitive scene (center) corresponds to *Ambiguous + shadow* setup from Fig. 7 with asymmetric lightning that creates shadows in the scene, ambiguous scene (right) corresponds to *Ambiguous* setup from Fig. 7 with complete ambiguity in the scene.

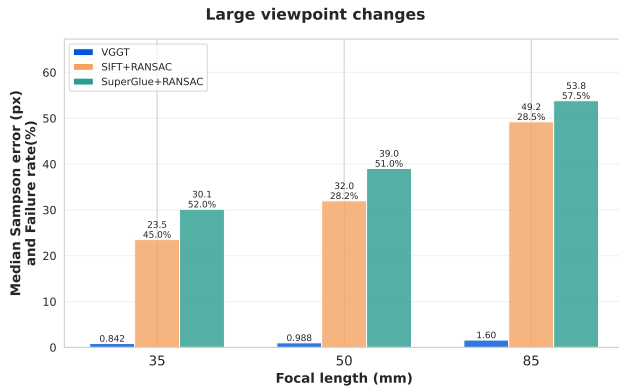


Figure 9. **Robustness to focal length changes.** VGGT maintains stable performance while classical baselines exhibit high failure rates.

6. Discussion

Our geometric analysis provides evidence that VGGT encodes epipolar structure within its intermediate layers. A closer examination of these layers shows that several attention heads also capture point correspondences across two views. The strong alignment between these emergent correspondences and the geometric constraints suggests that VGGT organizes information (at least partially) geometrically. Intervening on the most involved attention heads confirmed their functional role in encoding geometry.

Our analysis of learned data priors reveals that VGGT partially fills in missing correspondences in scenes with occlusions. While input perturbations degrade both correspondence matching and geometric accuracy, the degradation is not significant. Particularly, the correspondence matching performance remains above zero in the occluded patches. The latter shows that the model hallucinates missing correspondences instead of ignoring them. This is potentially unwanted behavior, as the purpose of this model is reconstruction and not generation.

We speculate these hallucinations stem from a learned data prior. While one could argue that hallucinations, if correct, are a desired property of a 3D reconstruction model,

however, it is impossible to resolve the inherent single-view ambiguity when one of the two images is occluded. We thus consider this behavior undesirable.

VGGT further demonstrates superior robustness compared to classical methods on scenarios where local feature ambiguity causes traditional pipelines to fail. The model’s global processing enables it to leverage subtle cues, such as shadows, that classical methods are not able to use.

While these findings suggest VGGT has learned robust geometric principles, we cannot claim it implements any specific classical algorithm. The model likely relies on a mixture of learned heuristics, explicit point correspondences, and some form of geometric algorithm.

Limitations. Our study focuses on synthetic data and certain camera configurations, so generalization to fundamentally different geometric and scene configurations remains unclear. Further, some traditional methods, like SIFT, struggle with large texture-less areas in synthetic data, which confounds conclusions about relative performance in a general experimental setting. Finally, our intervention analysis reveals the causal relationship between certain attention heads that encode correspondence matching and epipolar geometry, but our interventions were not local enough to claim that it is indeed the correspondences in these heads that make this relationship. Although unlikely, there could be other hidden mechanisms in the same attention heads that cause epipolar geometry.

7. Conclusion

We presented a systematic study of the VGGT model to determine whether it employs interpretable geometric concepts or relies only on learned appearance-based priors. Our results show that VGGT does encode geometric structure and they strongly indicated that it uses point correspondences to do so. Further, our input perturbation experiments reveal that the model strongly relies on learned priors, which provide robustness to input variations but can also sometimes lead to undesirable hallucinations.

Acknowledgments

This research was funded by the German Research Foundation (DFG) 417962828, 539134284 and 499552394 (SFB 1597 - Small Data), and by the German Ministry for Economy and Climate Protection via a decision by the German parliament (19A23014R). The research visit within the ELIS PhD program was supported through the ELSA mobility program. We want to thank Jianyuan Wang, Paul Englester, Orest Kupyn, Simon Schrodi, Karim Farid, and Rajat Sahay for valuable discussions and feedback during the development of this work.

References

- [1] Sameer Agarwal, Yasutaka Furukawa, Noah Snavely, Ian Simon, Brian Curless, Steven M Seitz, and Richard Szeliski. Building rome in a day. *Communications of the ACM*, 54(10):105–112, 2011. 2
- [2] Guillaume Alain and Yoshua Bengio. Understanding intermediate layers using linear classifier probes, 2018. 2
- [3] David Bau, Bolei Zhou, Aditya Khosla, Aude Oliva, and Antonio Torralba. Network dissection: Quantifying interpretability of deep visual representations. In *Computer Vision and Pattern Recognition*, 2017. 2
- [4] David Bau, Jun-Yan Zhu, Hendrik Strobelt, Agata Lapedriza, Bolei Zhou, and Antonio Torralba. Understanding the role of individual units in a deep neural network. *Proceedings of the National Academy of Sciences*, 2020. 2
- [5] Yonatan Belinkov, Nadir Durrani, Fahim Dalvi, Hassan Sajjad, and James Glass. What do neural machine translation models learn about morphology? In *Proceedings of the 55th Annual Meeting of the Association for Computational Linguistics (ACL)*, Vancouver, 2017. Association for Computational Linguistics. 2
- [6] Angel X. Chang, Thomas Funkhouser, Leonidas Guibas, Pat Hanrahan, Qixing Huang, Zimo Li, Silvio Savarese, Manolis Savva, Shuran Song, Hao Su, Jianxiong Xiao, Li Yi, and Fisher Yu. ShapeNet: An Information-Rich 3D Model Repository. Technical Report arXiv:1512.03012 [cs.GR], Stanford University — Princeton University — Toyota Technological Institute at Chicago, 2015. 1, 3
- [7] Hila Chefer, Shir Gur, and Lior Wolf. Transformer interpretability beyond attention visualization. In *Proceedings of the IEEE/CVF Conference on Computer Vision and Pattern Recognition (CVPR)*, pages 782–791, 2021. 2
- [8] Nelson Elhage, Neel Nanda, Catherine Olsson, Tom Henighan, Nicholas Joseph, Ben Mann, Amanda Askell, Yuntao Bai, Anna Chen, Tom Conerly, Nova DasSarma, Dawn Drain, Deep Ganguli, Zac Hatfield-Dodds, Danny Hernandez, Andy Jones, Jackson Kernion, Liane Lovitt, Kamal Ndousse, Dario Amodei, Tom Brown, Jack Clark, Jared Kaplan, Sam McCandlish, and Chris Olah. A mathematical framework for transformer circuits. *Transformer Circuits Thread*, 2021. <https://transformer-circuits.pub/2021/framework/index.html>. 2
- [9] Martin A Fischler and Robert C Bolles. Random sample consensus: a paradigm for model fitting with applications to image analysis and automated cartography. *Communications of the ACM*, 24(6):381–395, 1981. 2
- [10] Mor Geva, Jasmijn Bastings, Katja Filippova, and Amir Globerson. Dissecting recall of factual associations in autoregressive language models. In *Proceedings of the 2023 Conference on Empirical Methods in Natural Language Processing*, 2023. 5
- [11] R.I. Hartley. In defense of the eight-point algorithm. *IEEE Transactions on Pattern Analysis and Machine Intelligence*, 19(6):580–593, 1997. 2
- [12] R. I. Hartley and A. Zisserman. *Multiple View Geometry in Computer Vision*. Cambridge University Press, ISBN: 0521540518, second edition, 2004. 2, 1
- [13] Stefan Heimersheim and Neel Nanda. How to use and interpret activation patching, 2024. 2
- [14] Iro Laina, Yuki M Asano, and Andrea Vedaldi. Measuring the interpretability of unsupervised representations via quantized reversed probing. In *International Conference on Learning Representations*, 2022. 2
- [15] Vincent Leroy, Yohann Cabon, and Jerome Revaud. Grounding image matching in 3d with mast3r. In *ECCV*, 2024. 1, 2
- [16] Philipp Lindenberger, Paul-Edouard Sarlin, and Marc Pollefeys. LightGlue: Local Feature Matching at Light Speed. In *ICCV*, 2023. 2
- [17] David G Lowe. Distinctive image features from scale-invariant keypoints. *International journal of computer vision*, 60(2):91–110, 2004. 2, 6, 7
- [18] Dominic Maggio, Hyungtae Lim, and Luca Carlone. Vggt-slam: Dense rgb slam optimized on the sl(4) manifold, 2025. 2
- [19] D. Nister. An efficient solution to the five-point relative pose problem. *IEEE Transactions on Pattern Analysis and Machine Intelligence*, 26(6):756–770, 2004. 2
- [20] Catherine Olsson, Nelson Elhage, Neel Nanda, Nicholas Joseph, Nova DasSarma, Tom Henighan, Ben Mann, Amanda Askell, Yuntao Bai, Anna Chen, Tom Conerly, Dawn Drain, Deep Ganguli, Zac Hatfield-Dodds, Danny Hernandez, Scott Johnston, Andy Jones, Jackson Kernion, Liane Lovitt, Kamal Ndousse, Dario Amodei, Tom Brown, Jack Clark, Jared Kaplan, Sam McCandlish, and Chris Olah. In-context learning and induction heads. *Transformer Circuits Thread*, 2022. <https://transformer-circuits.pub/2022/in-context-learning-and-induction-heads/index.html>. 2
- [21] Paul D Sampson. Fitting conic sections to “very scattered” data: An iterative refinement of the bookstein algorithm. *Computer graphics and image processing*, 18(1):97–108, 1982. 3
- [22] Paul-Edouard Sarlin, Daniel DeTone, Tomasz Malisiewicz, and Andrew Rabinovich. SuperGlue: Learning feature matching with graph neural networks. In *CVPR*, 2020. 2, 6, 7
- [23] Johannes L. Schönberger and Jan-Michael Frahm. Structure-from-motion revisited. In *2016 IEEE Conference on Computer Vision and Pattern Recognition (CVPR)*, pages 4104–4113, 2016. 2

- [24] Noah Snavely, Steven M. Seitz, and Richard Szeliski. *Photo tourism: exploring photo collections in 3D*. Association for Computing Machinery, New York, NY, USA, 1 edition, 2023. [2](#)
- [25] Michal Stry, Julien Gaubil, Ayush Tewari, and Vincent Sitzmann. Understanding multi-view transformers, 2025. [2](#)
- [26] Jiaming Sun, Zehong Shen, Yuang Wang, Hujun Bao, and Xiaowei Zhou. LoFTR: Detector-free local feature matching with transformers. *CVPR*, 2021. [2](#)
- [27] Jianyuan Wang, Nikita Karaev, Christian Rupprecht, and David Novotny. Vggsfm: Visual geometry grounded deep structure from motion. In *CVPR*, 2024. [2](#)
- [28] Jianyuan Wang, Minghao Chen, Nikita Karaev, Andrea Vedaldi, Christian Rupprecht, and David Novotny. Vggt: Visual geometry grounded transformer. In *CVPR*, 2025. [1](#), [2](#), [3](#)
- [29] Shuzhe Wang, Vincent Leroy, Yohann Cabon, Boris Chidlovskii, and Jerome Revaud. Dust3r: Geometric 3d vision made easy. In *CVPR*, 2024. [1](#), [2](#)
- [30] Jianing Yang, Alexander Sax, Kevin J. Liang, Mikael Henaff, Hao Tang, Ang Cao, Joyce Chai, Franziska Meier, and Matt Feiszli. Fast3r: Towards 3d reconstruction of 1000+ images in one forward pass. In *Proceedings of the IEEE/CVF Conference on Computer Vision and Pattern Recognition (CVPR)*, 2025. [2](#)
- [31] Fred Zhang and Neel Nanda. Towards best practices of activation patching in language models: Metrics and methods. In *International Conference on Representation Learning*, pages 1651–1678, 2024. [2](#)
- [32] Bolei Zhou, Yiyou Sun, David Bau, and Antonio Torralba. Interpretable basis decomposition for visual explanation. In *Proceedings of the European Conference on Computer Vision (ECCV)*, 2018. [2](#)
- [33] Dong Zhuo, Wenzhao Zheng, Jiahe Guo, Yuqi Wu, Jie Zhou, and Jiwen Lu. Streaming 4d visual geometry transformer. *arXiv preprint arXiv:2507.11539*, 2025. [2](#)

On Geometric Understanding and Learned Data Priors in VGGT

Supplementary Material

A. Dataset generation details

We generated a controlled synthetic dataset from ShapeNet [6] assets rendered in Blender. We opted for a simpler synthetic dataset with complete control over the scenes since complex scenes with ambiguity could bias our analysis of the model’s internal workings. Each scene was rendered with different camera configurations regarding focal length, angular distance between the cameras, and scene composition.

We selected 13 different categories (bag, basket, bathtub, bed, bench, bottle, bowl, cap, car, chair, earphone, jar), where we define splits of *unique* assets with distinctive features and *symmetric* assets with object symmetry (basket, bottle, bowl, jar). For each category, we define splits for the probing experiment: 15 instances for training, 2 for validation, and 2 for testing, for a total of 10 categories (bottles, bowls, and symmetric jars are omitted).

We further define smaller and larger testing splits, which we use for experiments in Sec. 4 and Sec. 5. Both testing splits are a combination of validation and testing splits used in the probing experiment. For the smaller version, we include only 5 instances from 5 categories (bed, cap, car, chair, and jar). For the larger version, we include all instances from the validation and training splits, resulting in 40 instances across 10 categories. Finally, we also define another split with fully symmetric objects from the categories basket, bottle, bowl, and jar, which we use to create repetitive scenes.

We generated the data in Blender by positioning the object at the origin and sampling five camera pairs in the scene. We first randomly chose a position of the first camera, and based on the selected camera configuration mode, we defined the position of the second camera in the scene. We rendered the scenes with different focal lengths (24 mm, 35 mm, 40 mm, 50 mm, 70 mm, 85 mm, 100 mm) and a sensor size of 36 mm, where larger focal lengths result in *zoomed in* images. We calculated ground truth data for pair combinations in both directions (camera 1-camera 2 and camera 2-camera 1) with ground truth data including camera poses, correspondences, and fundamental matrix.

We included four camera configurations: a stereo camera pair with parallel image planes and a horizontal baseline, and non-parallel image planes with different angles between the cameras marked as small (10 - 25 degrees), medium (45 - 75), and large (90 - 120). Viewpoint differences present one aspect of task difficulty.

B. Probing VGGT for geometry

We probe VGGT’s intermediate representation to uncover where and how the geometry is represented. We use only the camera token, since VGGT’s camera head uses the final-layer camera token.

We train simple two-layer MLP probes on VGGT’s camera tokens at each layer to predict the fundamental matrix. Each probe uses a hidden dimension of 512 and is optimized for 50 epochs using the Adam optimizer with a learning rate of $1e-4$, and a step scheduler with a step size of 10 and a gamma of 0.5. We use the Sampson distance (in square-pixel space) as the training loss over all available ground-truth correspondences, without directly enforcing the rank-2 constraint. We train probes on a mixture of all four camera configurations and seven focal lengths, using a train split with 10 categories, as mentioned earlier in Sec. A. We report the root Sampson error in pixel space across 4 unseen data splits: val and test splits containing training categories in novel scenes (20 scenes in each split); novel objects (5 scenes) containing unseen categories, and symmetric objects (7 scenes) containing fully symmetric unseen scenes.

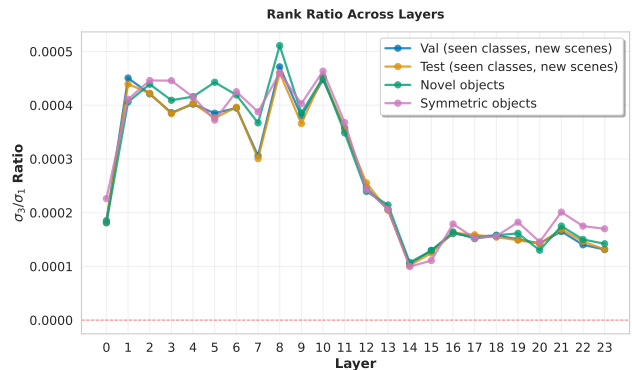


Figure 10. **Rank ratio.** Ratio of smallest and largest singular values across layers on different data splits for the probing experiment from Fig. 2. A good fundamental matrix should have a significant difference between the largest and smallest singular values.

Figure 2 shows that middle layers (around layer 12) comprise a representation that allows for fundamental matrix F recovery, which is seen by a sudden drop in Sampson distance error. Here, on Fig. 10, we show another criterion for evaluating the fundamental matrix – the ratio between the smallest and largest singular values of the fundamental matrix. Since the fundamental matrix is of rank 2 [12], its smallest singular value should be around zero, and the largest singular value should be significantly larger for a

well-estimated fundamental matrix. We observe minimum values in the same set of layers where the sudden drop occurs, with a significant difference between them in the final layers. This further supports the emergence of epipolar geometry by satisfying the rank-2 constraint without directly enforcing it during probe training.

C. Correspondence matching in attention maps

We analyze the attention maps of the VGGT’s global attention layers for correspondence matching capabilities. Precisely, we analyze the query-key (QK) attention space after softmax, where for each pair of corresponding patches (patch from the first image and its corresponding patch in the second image and vice versa), we look for the location in the attention map with the highest value and calculate the accuracy whether the patch with highest accuracy corresponds to the true matching patches or not. Since the patches are 14×14 pixels, there will be scenarios in which a patch from the first image has multiple matches in the second image. In such a case, we count a hit if any of the correct positions receives the highest attention value. For a two-image sequence of dimension 518×518 we will have attention maps of dimension $(16, 2748, 2748)$ where 16 is the number of heads, and 2748 is the total length of tokens in a sequence with 1374 tokens coming from the first image (1 camera token, 4 register tokens, 1369 image patch tokens) and final 1374 tokens from the second image.

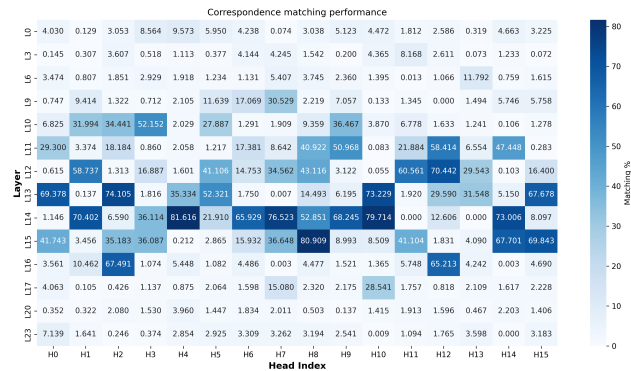


Figure 11. **Correspondence matching per attention head.** We observe the same trend as in Fig. 3 when calculating the correspondence matching from the second image into the first image in the sequence. Some slight differences occur, but the general trend is the same.

Figure 3 shows the average correspondence accuracy when calculating the matching from the first image in the sequence to the second image in the sequence, and we observe middle layers having strong correspondence matching capabilities in multiple heads. Here, on Fig. 11, we show the average correspondence accuracy when calculating the

matching from the second image in the sequence to the first one, which means we are just using different query indices of the second image and key indices of the first image for the calculation. We again observe the same trend with middle layers showing strong matching performance.

There are, however, slight differences in the matching percentages for certain heads, coming from an asymmetric attention space, which is probably due to the first image in the sequence being treated as the reference frame, and thus attention maps being almost, but not completely, symmetric.

D. Causal role of attention patterns

To determine whether the previously identified attention patterns in the middle layers are truly the cause of the geometric understanding, we perform targeted interventions on the attention heads. In Fig. 4 we show results for only five combinations of layers and heads, but here, in Fig. 12 we present more combinations of layers and heads on which we intervene. All combinations are chosen based on the layer’s matching performance, where we select the strongest matching heads to intervene on.

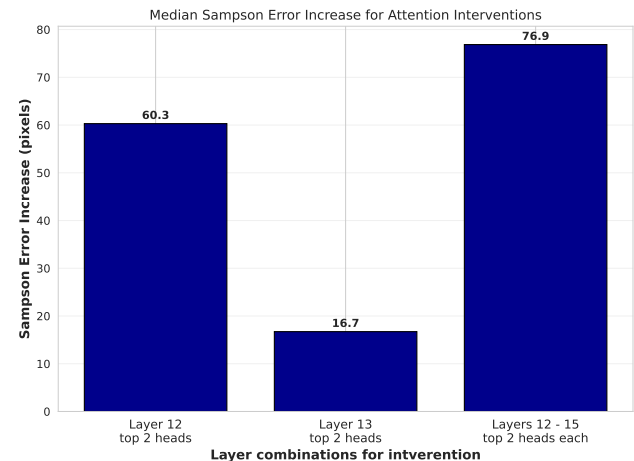


Figure 12. **Performance degradation under attention interventions.** Disrupting early or late layers has minimal impact on performance, whereas middle-layer interventions cause significant degradation. Even two heads in a single layer with strong correspondence matching suffice to impair geometric understanding.

We present 3 new combinations of strong matching heads in the middle layers (12-15). We clearly see that when intervening on the heads with strong matching capabilities, we observe a significant drop in performance.

Further, our current intervention technique is not entirely local, as we set the entire attention map for all patches to zero, regardless of whether they have corresponding relations. This could, in fact, bias our results as the degradation is not entirely due to the correspondence matching

capability, but perhaps these heads and layers could be performing additional tasks at the same time. Thus, we perform an additional intervention that localizes the intervention only to the patches with a clear corresponding relation. This means that for the patches in the first image, we zero out the complete attention map of the second image only if the patch has a correspondence in the second image. We do the same for the patches in the second image and zero out the attention map of the first image. We show the results in Fig. 13, where we observe the same trend as earlier, now with stronger results indicating that middle layers with correspondence-matching capabilities are important for geometric understanding.

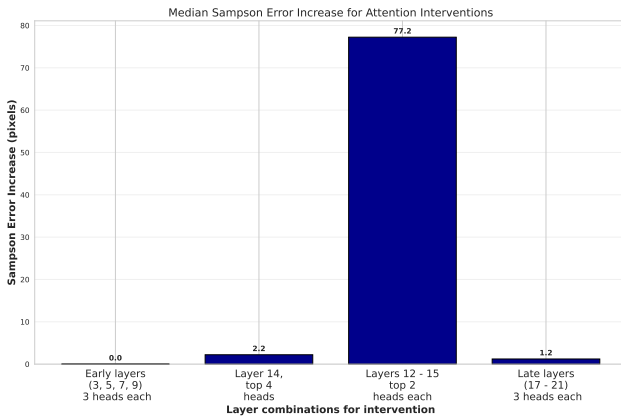


Figure 13. **Performance degradation under attention interventions by intervening on the whole attention map of the corresponding patches.** Disrupting middle layers causes significant degradation.

And finally, we localize the interventions to target only the corresponding patches directly in the attention maps. Now, we zero out only the patches where we expect the highest attention values and recalculate the softmax values. In this case, we do not *delete* the whole attention map of the image, but introduce missing correspondence matches. We show the results in Fig. 14, where we again observe performance degradation when intervening directly on the correspondences, but of less intensity. **This now further supports the relation between the correspondence matching in the middle layers and geometric understanding.**

E. VGGT’s robustness to scene modifications

In Sec. 5 we test VGGT’s performance across different scenes and input modifications, demonstrating that it outperforms both standard and learned methods.

Occlusion experiments We provide more visual examples of the occlusion experiment described and performed in Fig. 5. In Fig. 15 we show 3 pairs of input images where

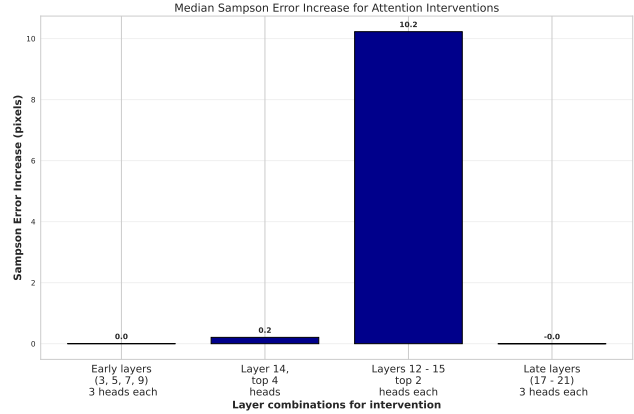


Figure 14. **Performance degradation under attention interventions by intervening only on the corresponding patches in the attention maps.** Disrupting early or late layers has minimal impact on performance, whereas middle-layer interventions cause significant degradation.

the second image in the sequence is occluded with white patches. The red patch in the middle of each occluded area represents the patch used for the calculation of the number of matching heads before and after the intervention.

Lightning changes We compare VGGT’s performance against SuperGlue and RANSAC in Fig. 6. Here, in Fig. 16, we demonstrate how the tested modifications appear in a single scene. In general, VGGT is quite robust, but we observe significant Sampson distance errors for combinations with top-view, rainbow, and neon lighting. In such modifications, shadows in the scene are disturbed.

Focal length changes Focal length changes effectively zoom in or out of the scene, changing the correspondence difficulty. We test focal lengths from 24 mm to 100 mm (36 mm sensor) across different viewpoint difference configurations. In Fig. 9 we show results for large viewpoint differences between the cameras (90 - 120 degrees), while here, in Fig. 17 we show the results for other camera configurations based on viewpoint differences. We observe a slight difference in results when the viewpoint difference between the cameras is small, but VGGT performs much better on larger viewpoint differences.



Figure 15. Examples of occlusion experiment where the second image from the pair is occluded with white patches. Red patches in the middle of each occluded area represent the patches used for the calculation of the matching head metrics, as shown in Fig. 5.



Figure 16. Examples of the light and color modifications used in Fig. 6 over one scene.

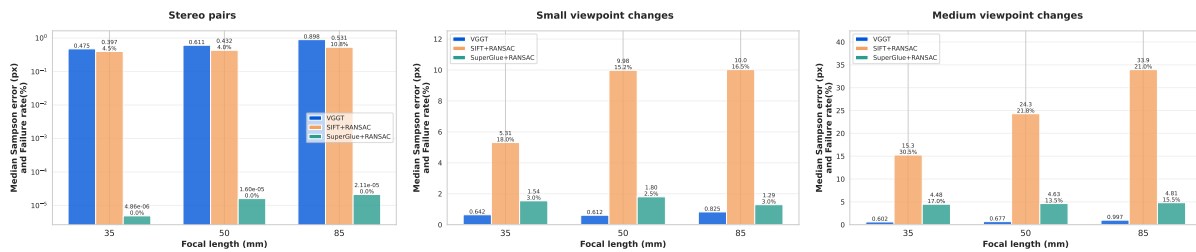


Figure 17. **Robustness to focal length changes for different viewpoint differences between the cameras.** VGGT outperforms the baselines for the case of large viewpoint differences, but performs on par with the baselines for stereo pair cameras.